Permian-Triassic redox shift and its ferruginous aftermath in epicontinental seas

Fen Yang[1,2], Sen Li[3]*, Stephen E. Grasby[4], David Bond[5], Ming Pan[1,2], Yadong Sun[3]

[1] Institute of Karst Geology, CAGS/Key Laboratory of Karst Dynamics, MNR & GZAR/International Research Center on Karst under the Auspices of UNESCO, Guilin, Guangxi 541004, China 541004, China.

[2] Pingguo Guangxi, Karst Ecosystem, National Observation and Research Station, Pingguo, Guangxi 531406, China.

[3] State Key Laboratory of Geomicrobiology and Environmental Changes, China University of Geosciences, Wuhan 430074, China.

[4] Geological Survey of Canada, 3303-33rd Street NW, Calgary, Alberta T2L 2A7, Canada.

[5] School of Environmental and Life Sciences, University of Hull, Hull, HU6 7RX, United Kingdom.

Correspondence to: Sen Li (lisen@cug.edu.cn)

Abstract. Marine anoxia has been implicated as a key environmental driver of the end-Permian mass extinction (EPME) and the subsequent prolonged recovery. However, the spatial and temporal extent of oxygen limitation during the EPME interval remains contentious. Here, we present iron speciation, pyrite framboid and molybdenum-uranium (Mo-U) covariation data from two palaeogeographically distinct settings: the Tethyan Chibi section (South China) and the Panthalassian Ursula Creek section (Western Canada) to evaluate redox dynamics across the Permian-Triassic transition. Our data suggest that bottom waters were predominantly dysoxic during the late Changhsingian at both sites. Later, the prevalence of small pyrite framboids, elevated Mo and U enrichment factors (Mo_{EF} and U_{EF}), and high Mo_{EF}/U_{EF} ratios near the EPME horizon implicate seafloor anoxia as a key trigger for marine extinctions in the Ursula Creek section. In the post-extinction Early Triassic, iron speciation and Mo_{EF}-U_{EF} covariation data reveal a shift to persistently ferruginous conditions in both locations. A global compilation of iron speciation data indicates redox variation between ferruginous and euxinic conditions in epicontinental seas during the Permian-Triassic crisis, with ferruginous conditions expanding significantly in the earliest Triassic. The expansion of a ferruginous seafloor would have limited phosphorus bioavailability, suppressing primary productivity in the immediate aftermath of the EPME, thereby contributing to the slow recovery.

1 Introduction

The end-Permian mass extinction (EPME), ca. 252 Ma, stands as the Phanerozoic's most profound biodiversity crisis and results in a major turnover from Paleozoic to Mesozoic ecosystems (Sepkoski, 1981; Erwin, 2006; Fan et al., 2020). An extreme greenhouse climate prevailed during the Early Triassic (López-Gómez et al., 2005; Joachimski et al., 2012; Sun et al., 2012; Medici et al., 2019), accompanied by extensive oxygen depletion (Isozaki, 1997; Lau et al., 2016; Wu et al., 2024). The post-extinction recovery of marine ecosystems was protracted and punctuated by a series of aborted recoveries, initially characterized by low-complexity communities dominated by calcimicrobes and sparse, low-diversity metazoans. Opportunistic taxa (e.g., small gastropods and bivalves) proliferated globally (Pruss et al., 2006; Chen and Benton, 2012; Foster and Twitchett, 2014; Pietsch et al., 2019).

Marine anoxia has been widely considered a primary mechanism driving the EPME and the subsequent slow, punctuated biotic recovery (Wignall and Hallam, 1992; Grasby et al., 2013; Lau et al., 2016; Hülse et al., 2021). Several hypotheses describe the spatio-temporal patterns of oxygen depletion during the EPME. These include the development of global "superanoxia" (Isozaki, 1997; Wignall and Twichett, 2002; Isozaki, 2009), the stratification of oceans into oxic surface waters and euxinic (H_2S-rich) deep waters (e.g., Kump et al., 2005; Meyer et al., 2008), the expansion of euxinic oxygen minimum zones (OMZs) at intermediate water depths (~200–1000 m) while deep-ocean redox conditions remained largely unchanged (Algeo et al., 2010, 2011; Winguth and Winguth, 2012), and the expansion of ferruginous [Fe(II)-rich, non-euxinic] conditions (Clarkson et al., 2016; Zhang et al., 2024). In deep-water settings of Panthalassa (e.g., the rare records from Japan and New Zealand), evidence such as small pyrite framboids (mean diameters < 5 μm), significant enrichment of redox-sensitive trace elements (e.g., Mo), and negative pyrite sulfur isotope shifts has been interpreted to indicate either persistent euxinia (Shen et al., 2011; Takahashi et al., 2021) or euxinia largely restricted to OMZs, with bottom waters remaining dysoxic to suboxic (Algeo et al., 2010, 2011). Numerous studies demonstrate that euxinic waters invaded shallow epicontinental basins extensively around the Permian-Triassic (P-T) boundary, including equatorial Tethys (e.g., the South China Craton), the Gondwanan margin in mid to high latitudes, and the Pangaea northwestern margin (Wignall and Twitchett, 1996; Grasby and Beauchamp, 2008; Neilsen et al., 2010; Lau et al., 2016; Zhang et al., 2017; Stebbins et al., 2019; Xiang et al., 2020). In addition, studies of the Nhi Tao section in Vietnam documented multiple recurrent incursions of

euxinic water masses onto a tropical shallow-marine carbonate platform during the earliest Triassic, likely linked to episodic upwelling of sulfidic deep waters (Algeo et al., 2007, 2008). Biomarker evidence from chlorobactene (indicative of green sulfur bacteria) also suggests that euxinic waters expanded into the photic zone (Grice et al., 2005; Cao et al., 2009).

Iron proxies provide additional redox information, distinguishing euxinic and ferruginous conditions during the EPME. Along the margins of equatorial Tethys (e.g., South China), iron proxies document a shift from the Changhsingian euxinic to Griesbachian ferruginous conditions, as indicated by the decreased ratio of pyrite iron over the highly reactive iron pool (Fe_{py}/Fe_{HR}) in multiple sections (Xiang et al., 2016, 2020; Lei et al., 2017; Ge et al., 2022; Yang et al., 2024). Conversely, strata from the northwestern Pangaea margin reveal a different redox trend, with ferruginous conditions transitioning to euxinic environments across the P-T boundary (e.g., Neilsen et al., 2010; Mettam et al., 2017; Schobben et al., 2020). Meanwhile, Panthalassa experienced predominantly euxinic conditions across the EPME, with intermittent ferruginous intervals developing during the earliest Triassic (Takahashi et al., 2021).

Evidence increasingly suggests that anoxia may have been largely confined to slope settings, with periodic redox oscillations driving transient anoxic episodes in shallow marine environments (Algeo et al., 2007, 2008; Shen et al., 2012, 2016; Zhang et al., 2017). Independent proxies—including bioturbation, depletion of Fe_{HR}, absence of pyrite framboids, rare earth element anomalies, and Mo and Tl isotope signatures—indicate intervals with sustained oxygenation of bottom waters regionally around the EPME (Beatty et al., 2008; Proemse et al., 2013; Garbelli et al., 2016; Newby et al., 2021; Chen et al., 2022; Ge and Bond, 2022; Taniwaki et al., 2022; Yang et al., 2024; Frank et al., 2025). These findings suggest that oxygen restriction during the EPME was spatially heterogeneous. While oxic refugia can be reconciled with U-based modelling that suggests only ~20% of the seafloor was anoxic at that time (Lau et al., 2016), there remains an issue that the residence time of U in seawater would not capture transient anoxic events (Grasby et al., 2021).

To better constrain marine redox dynamics in epicontinental seas during the P-T transition under extreme climatic conditions, this study investigates two Upper Permian to Lower Triassic successions from contrasting palaeogeographic settings: Chibi (equatorial Tethys) and Ursula Creek (northwestern margin of Pangaea). Specifically, this study aims to: (i) characterize the spatio-temporal evolution of redox conditions across this transition using integrated iron speciation, framboid morphology, and Mo-

U covariation data; and (ii) evaluate regional differences and broader patterns in redox shifts (euxinic vs. ferruginous).

2 Geological settings

The P-T interval corresponds to the final assembly of Pangaea, which was centered near the equator and extended across nearly all latitudes, surrounded by the Panthalassa Ocean (Scotese, 2014). This large-scale continental amalgamation marked the termination of the Late Paleozoic Ice Age and the transition to greenhouse climatic conditions (Crowell, 1995; Chen et al., 2018). Contemporaneously, extensive large igneous province volcanism, including the Emeishan Large Igneous Province and the Siberian Traps, peaked around the P-T boundary (He et al., 2007; Burgess and Bowring, 2015).

Paleogeographic reconstructions indicate that the South China Craton was situated in the equatorial eastern Tethys and remained tectonically isolated during the P-T interval (Scotese, 2014; Fig. 1A). And it's bounded by several major tectonic units, including the Ailaoshan–Songma suture zone, the Jinshajiang suture, the Longmenshan Thrust Belt, and the Qinling–Dabie–Sulu orogen (Wan, 2012; Cawood et al., 2018). This tectonic regime persisted until the Middle Triassic, when collision with the Simao–Indochina blocks initiated orogenesis (e.g., Wang et al., 2018). The well-preserved P-T boundary successions in South China have been linked to this relatively stable, extension-dominated setting. During the latest Permian (Changhsingian), sedimentation across the South China Craton was characterized by a pronounced platform-basin differentiation, with shallow-water carbonate deposition dominating the Yangtze Platform and siliceous deep-water sediments accumulating along its margins (Feng et al., 1996; Fig. 1B). The Chibi section (29°45′5.33″N, 113°57′6.75″E) is exposed in the northern marginal basin of the middle Yangtze Platform. It records a continuous P-T stratigraphic succession, encompassing the Wuchiaping and Talung formations (Upper Permian) and extending upward into the Daye Formation (Lower Triassic) (Yang et al., 2022). The Wuchiaping Formation comprises grey, thick-bedded wackestones and packstones containing abundant benthic calcareous bioclasts and chert nodules. It is overlain by the Talung Formation, which is characterized by thin-bedded cherts interbedded with siliceous mudstones, wackestones, and shales and commonly yields radiolarians and sponge spicules. The overlying Daye Formation consists mainly of thin-bedded wackestones interlayered with marls, and the P-T boundary is located 83 cm above its basal contact (Yang et al., 2022).

On the northwestern margin of Pangaea, the Canadian Cordillera developed from remnants of Rodinia (~750 Ma) and attained its present configuration by the Late Cretaceous (Monger and Price, 2002). During the Late Permian, this region was situated at mid-latitudes (~30°N) along a passive continental margin facing the Panthalassa Ocean (Fig. 1A; Zelt et al., 2006). The Ursula Creek section (55°59′36.54″N, 123°10′27.18″W) is located on the north shore of Williston Lake, a hydroelectric reservoir in British Columbia in the Canadian Rocky Mountains (Fig. 1C). Previous studies have documented the stratigraphic characteristics of the Ursula Creek section, a deep marine succession that exposes near-vertically dipping strata spanning the Middle Permian to Middle Triassic (Henderson, 1997; Woods et al., 2023). Upper Permian-Lower Triassic strata are assigned to the Fantasque and Grayling formations. The Fantasque Formation is composed predominantly of thin-bedded cherts intercalated with shale layers, and its faunal assemblages are characterized by abundant radiolarians and sponge spicules. The overlying Grayling Formation comprises thinly bedded shales. The P-T boundary was identified at ~80 cm above the base of the Grayling Formation (Wignall and Newton, 2003).

3 Methods

3.1 Pyrite framboids

Size distributions of pyrite framboids were determined from 37 prepared thin sections at Ursula Creek using a scanning electron microscope (SEM) at the State Key Laboratory of Geomicrobiology and Environmental Changes, China University of Geosciences (CUG Wuhan). All polished thin sections were sputter-coated with carbon powder to enhance imaging quality. The SEM was operated in backscattered electron mode at 2500 × magnification. The chemical composition of framboids was qualitatively characterized using energy-dispersive spectroscopy (EDS).

3.2 Iron speciation

For iron proxies, 97 bulk rock samples from the Chibi and Ursula Creek sections were crushed with a jaw crusher and ground by a mixer mill. Total iron (Fe_T) concentrations were determined using X-ray fluorescence (XRF) at the ALS Minerals laboratory located in Guangzhou, achieving a reproducibility better than 0.1 wt% (1σ). Of these, 54 samples showing Fe_T values above 0.5 wt% were used in subsequent Fe speciation extractions. Iron phases associated with carbonates (Fe_{carb}), (oxyhydr)oxides

(Fe_{ox}), and magnetite (Fe_{mag}) were sequentially extracted following Poulton and Canfield (2005). Fe_{carb} was removed using 1M Na-acetate (pH 4.5) at 50 °C for 48 h, Fe_{ox} with Na-dithionite (pH 4.8) at room temperature for 2h, and Fe_{mag} with a solution of 0.2M ammonium oxalate and 0.17M oxalic acid at room temperature for 6h. Fe concentrations were determined using atomic absorption spectrometry at the State Key Laboratory of Geomicrobiology and Environmental Changes, CUG Wuhan. The Fe_{py} was quantified stoichiometrically determined by the weight of precipitated Ag_2S following chromous chloride distillation, as described by Canfield et al. (1986). Replicate extractions of the WHIT international reference material (Alcott et al., 2020) gave a relative standard deviation below 5% for each step.

3.3 Trace elements and enrichment factors calculation

For trace elements, 103 powdered samples were treated with a mixture of H_2O, HF, $HClO_4$, and HNO_3 (2:2:1:1) for digestion at the Geological Survey of Canada. Analyses of the resulting solutions were quantified by ICP-MS (PerkinElmer), and replicate measurements showed a relative deviation below 2% (2σ). Enrichment factors (EF) for trace elements were obtained by normalizing the X/Al ratios in samples to those of the Post-Archean Average Shale (PAAS; Taylor and McLennan, 1985), with X referring to Mo and U.

3.4 Framework for redox interpretations

Three redox methods, including pyrite framboid mean size, iron speciation, and Mo-U covariation, are applied in our study (e.g., Wilkin and Barnes, 1996; Algeo and Tribovillard, 2009; Poulton and Canfield, 2011). The abundance of pyrite framboids typically increases as anoxia develops, accompanied by a decrease in mean diameter and a narrowing of the size distribution. Specifically, the absence of framboids typically indicates local oxic conditions; abundant framboids with mean diameters ranging from 6 to 10 μm suggest dysoxic conditions while abundant framboids with mean diameters below 6 μm reflect anoxic environments, with those below 5 μm pointing to euxinic settings (e.g., Wilkin and Barnes, 1996; Bond and Wignall, 2010).

Iron speciation [e.g., Fe(II), Fe(III), and sulfide-associated phases] has been widely applied as a proxy to reconstruct palaeo-redox states (e.g., Poulton and Canfield, 2011). To ensure analytical reliability, these proxies are typically applied only to samples with Fe_T concentrations > 0.5 wt% (Clarkson et al., 2014). Oxic marine sediments typically exhibit low Fe_{HR}/Fe_T ratios (< 0.22), reflecting

limited authigenic Fe accumulation under well-oxygenated conditions (Poulton and Raiswell, 2002). By contrast, under anoxic environments, sediments commonly show substantial enrichment of Fe_{HR} ($Fe_{HR}/Fe_T > 0.38$; Poulton, 2021). Accumulation of H_2S in anoxic bottom waters promotes pyritization of Fe_{HR}, driving $Fe_{py}/Fe_{HR} > 0.8$, a threshold for euxinic settings. Conversely, $Fe_{py}/Fe_{HR} < 0.6$ is indicative of ferruginous settings, where H_2S availability is limited. When Fe_{py}/Fe_{HR} falls between 0.6 and 0.8, the redox classification becomes ambiguous and further evidence is required (e.g., from independent proxies) to make accurate redox interpretation (Poulton and Canfield, 2011).

Molybdenum-uranium covariation is widely used to reconstruct palaeo-redox states in ancient depositional environments, owing to their distinct redox-sensitive geochemical behaviors (e.g., Algeo and Tribovillard, 2009). The application of Mo_{EF} and U_{EF} to non-siliciclastic rocks is subject to potential artifacts, as low detrital Al content can result in abnormally high ratios (Tribovillard et al., 2006). Nevertheless, the consistent trends in EFs, concentrations, and their ratios in this study support their reliable application in redox analysis (Figs. 2 and 5). Generally, Both Mo and U show little or no enrichment under oxic and dysoxic condition, and low ratio in Mo/U (Algeo and Tribovillard, 2009; Tribovillard et al., 2012). While, under oxygen-depleted, non-euxinic conditions, both elements exhibit stronger enrichment (EFs > 10), with $Mo_{EF}/U_{EF} < 1 \times$ seawater. In contrast, under euxinic conditions, both elements could show strong enrichment (EFs > 10), and Mo is preferentially accumulated, leading to elevated Mo/U ratio (Algeo and Tribovillard, 2009; Tribovillard et al., 2012).

4 Results

4.1 Pyrite framboid analysis

At Ursula Creek, abundant pyrite framboids were observed in 20 of the 37 samples (54.1%; Fig. 2), totaling 2140 individuals measured for this study (see supplementary material). The remaining 17 samples contained either none, or rare pyrite framboids and euhedral pyrite.

Mean framboid diameters generally decrease upward in the Fantasque Formation (Fig. 2). Within the lowermost 3 m of the study section, three samples yield mean framboid diameters of 7.9–9.6 μm, with standard deviation (1 σ) ranging from 2.0 to 3.2 μm (Fig. 3). At section height 3–10 m, pyrite framboids are mostly absent except for one sample containing a small quantity (n = 55) of larger framboids (mean = 10.4 μm), a wide size distribution (3.6–25.3 μm), and a standard deviation of 4.7 μm.

Numerous framboids are observed within the upper interval of the Fantasque Formation (10–13 m section height), with mean diameters ranging from 6.8 to 9.6 μm and standard deviations between 2.1 and 3.5 μm. Mean diameters decrease slightly at the top of the Fantasque Formation (13–14.3 m section height), ranging from 5.7 to 6.5 μm, with narrow size distribution (1 σ < 3.0 μm). Within the basal ~2.7 m of the overlying Grayling Formation shales (earliest Griesbachian), framboids are absent. Above this interval, numerous small pyrite framboids exist in the Grayling Formation (17.5–31.6 m section height), with mean diameters between 5.3 and 6.5 μm and 1 σ from 1.2 to 2.8 μm. EDS analysis detected about 25 wt% oxygen content in pyrite framboids from the Ursula Creek section (Figs. 4A and B), suggesting partial oxidation rather than stoichiometric FeS_2.

4.2 Fe_T, Fe_T/Al and Fe proxies

At Ursula Creek, Fe_T contents range from 0.2 to 4.7 wt% (mean = 1.3 wt%), with 46 out of 59 samples exceeding 0.5 wt% (Fig. 2). Samples exhibiting Fe_T < 0.5 wt% occur exclusively in the lower Fantasque Formation (Fig. 2). Fe_T concentrations in the upper Fantasque Formation show a slight increase, varying from 0.5 to 1.1 wt% (mean = 0.7 wt%). The Grayling Formation exhibits generally higher Fe_T (0.5–4.7 wt%, mean = 2.2 wt%). In samples with Fe_T > 0.5 wt%, the Fe_{HR}/Fe_T is generally above 0.6 (mean = 0.9), with one exception of 0.3. The Fe_{py}/Fe_{HR} are low, varying from 0 to 0.7 (mean = 0.1). The Fantasque Formation shows consistently low Fe_{py}/Fe_{HR} ratios (mean = 0.2) while the Grayling Formation has more variable Fe_{py}/Fe_{HR} ratios (0–0.5, mean = 0.1). Notably, the Ursula Creek section records elevated Fe_{ox} contents, and Fe_{ox}/Fe_{HR} ratios span 0.1–0.9, with 28 of 35 values exceeding 0.5. The $(Fe_{ox}+Fe_{py})/Fe_{HR}$ ratios fall within 0.6–0.9 (mean = 0.8), with only two samples displaying values below 0.6. The total Fe relative to aluminum (Fe_T/Al) ratios vary from 0.1 to 2.7 (mean = 0.5), averaging 0.4 in the Fantasque Formation and 0.5 in the more variable Grayling Formation.

At Chibi, Fe_T concentrations vary from 0.1–5.7 wt% (mean = 1.1 wt%), with 25 samples showing values > 0.5 wt% (Fig. 5). Among these, 19 samples were analyzed for iron speciation. Most samples from the lower to middle Talung Formation (*C. subcarinata* and *C. changxingensis* zones) yield Fe_T < 0.5 wt%. Fe_T concentrations increase markedly in the upper Talung Formation (*C. yini-H. praeparvus* Zone), ranging from 0.9 to 5.7 wt%. The Daye Formation generally contained higher Fe_T concentrations than the Talung Formation, with most samples ranging from 0.5 to 2.6 wt% and two samples showing lower values. For samples with Fe_T > 0.5 wt%, Fe_{HR}/Fe_T ratios fall between 0.4 to 1.0 (mean = 0.7). The

Fe_{Py}/Fe_{HR} ratios in this section span 0.1–0.9 (mean = 0.4), with most values < 0.6 (14 out of 19 samples). Fe_{ox} contents are low, with Fe_{ox}/Fe_{HR} rations < 0.1 in all samples. The Fe_T/Al ratios fall between 0.4 and 6.7, (mean = 1.0) averaging 2.1 in the Talung Formation and a more stable 0.6 in the lower Daye Formation.

4.3 Molybdenum and uranium concentrations, enrichment factors and ratios

At Ursula Creek, Mo and U concentrations, their enrichment factors (Mo_{EF}, U_{EF}), and corresponding ratios (Mo/U, Mo_{EF}/U_{EF}) display similar variations, generally rising from the Late Permian into the Early Triassic (Fig. 2). In the Fantasque Formation (n = 34), Mo concentrations fall between 0.1 and 4.8 ppm (mean = 0.7 ppm), with corresponding Mo_{EF} values span 0.6 to 25.6 (mean = 4.3); most samples (n = 31) show only modest Mo enrichment (Mo_{EF} < 10). For U, concentrations fall in the range of 0.2–2.2 ppm (mean = 1.0 ppm), and U_{EF} values range from 1.6 to 17.7 (mean = 6.1). Mo_{EF}/U_{EF} ratios are generally low (0.2–2.2, mean = 0.6), with 25 samples exhibiting values below 0.1 times that of modern seawater, and the remainder falling in the range of 0.1 to 0.3 times seawater (Fig. 6A). In contrast, Mo/U ratios are relatively higher than Mo_{EF}/U_{EF} ratios, spanning 0.2–2.4 (mean = 0.7).

In the Grayling Formation (n = 41), all proxies exhibit significantly higher values. For Mo, concentrations and enrichment factors show significantly greater variation from 0.6 to 146.8 ppm (mean = 20.0 ppm) and 2.2 to 175.2 (mean = 29.1), respectively. Most samples (n = 36) show high Mo enrichment (Mo_{EF}: 11.0 to 57.0). One sample displays an extremely high enrichment (Mo_{EF} > 100), and four samples show low to modest enrichment (Mo_{EF} < 10). In contrast to Mo, U concentrations and enrichment factors exhibit modest variability, with concentrations varying narrowly from 1.3 to 15.0 ppm (mean = 6.0 ppm) and U_{EF} values ranging from 4.6 to 23.4 (mean = 9.9). Mo_{EF}/U_{EF} ratios fall between 0.4 and 8.9 (mean = 2.9). All but one sample have Mo_{EF}/U_{EF} ratios between 0.1 and 1 times that of modern seawater (Fig. 6A). Mo/U ratios span 0.5–9.8 (mean = 3.1).

At Chibi, Mo, U, Mo_{EF}, U_{EF}, Mo/U, and Mo_{EF}/U_{EF} generally decrease from the Late Permian into the Early Triassic, displaying an opposite trend to those at Ursula Creek (Fig. 5). In the Talung Formation, Mo exhibits stronger enrichment relative to U. Mo concentrations range from 13.8 to 67.6 ppm (mean = 19.7 ppm), and corresponding Mo_{EF} values range from 29.8 to 788.7 (mean = 229.7). U concentrations range from 2.3 to 15.1 ppm (mean = 6.3 ppm), with U_{EF} values between 16.8 and 428.8 (mean = 96.2). The Mo/U and Mo_{EF}/U_{EF} ratios range from 0.4 to 9.6 (mean = 3.6) and from 0.4 to 8.8 (mean = 3.3),

respectively. Most samples exhibit Mo_{EF}/U_{EF} ratios between 0.1 and 1 times that of modern seawater, whereas two samples exceed the modern seawater value and one sample falls below 0.1 times the modern seawater value (Fig. 6B).

In contrast, the Daye Formation is characterized by relatively stronger U enrichment compared to Mo. Mo concentrations range from 0.1 to 9.6 ppm (mean = 0.9 ppm), whereas U concentrations range from 0.6 to 43.0 ppm (mean = 5.3 ppm). Mo_{EF} values vary from 0.2 to 107.0 (mean = 8.7), and U_{EF} values range from 3.6 to 271.9 (mean = 35.5). The Mo/U and Mo_{EF}/U_{EF} ratios are consistently low and show limited variability, with both mean values and standard deviations of 0.2. All samples show Mo_{EF}/U_{EF} ratios < 0.1 times the modern seawater value (Fig. 6B).

5 Discussion

5.1 Redox evolution

Redox proxies from the Ursula Creek section indicate prolonged water-column deoxygenation during the Changhsingian at the northwestern margin of Pangaea. Abundant pyrite framboids with relatively large mean diameters (7.9 to 9.6 μm), and low Mo_{EF}/U_{EF} ratios (< 0.1 × seawater) in the basal ~3 meters of the studied Fantasque Formation indicate dysoxic conditions prevailed during deposition (Figs. 2 and 6; Bond and Wignall, 2010; Tribovillard et al., 2012). Though this interval is characterized by low Mo_{EF} (1.0 to 3.8) and low to modest U_{EF} (2.3 to 13.4), the low detrital Al component (0.6 to 2.4 wt%) typical for (bio)chemical sediments (e.g., chert and pure carbonate) results in EF values that appear higher than those in siliciclastic sediments (Tribovillard et al., 2006). From 3 to 8.5 m section height (Fantasque Formation), intense bioturbation, including ichnotaxa belonging to *Diplocraterion*, *Teichichnus*, and *Planolites*, along with low Mo_{EF} (0.7 to 9.0) and U_{EF} (1.9 to 7.1) values, low Al contents (0.6 to 2.5 wt%), low Mo_{EF}/U_{EF} ratios (< 0.1 × seawater), and a general lack of pyrite framboids suggests that oxic to dysoxic bottom waters were established during this part of the Changhsingian (Wignall and Newton, 2003; Fig. 2). Several samples that lack pyrite framboids at a height of 8.5–10 m exhibit Fe_{HR}/Fe_T > 0.38, moderately elevated Mo_{EF} (17.4 to 25.6) and U_{EF} (11.7–17.7), with Mo_{EF}/U_{EF} ratios spanning 0.1 to 0.3 times that of seawater, suggestive of anoxic conditions. Considering partial pyrite oxidation detected by EDS (Fig. 4A), it is possible that using Fe_{py}/Fe_{HR} could result in an underestimation of the presence of euxinic conditions, and therefore $(Fe_{ox} + Fe_{py})/Fe_{HR}$ is used to detect potential H_2S

accumulation on the seafloor. Consistently low (Fe_{ox} + Fe_{py})/Fe_{HR} values and elevated Fe_{HR}/Fe_T in this interval are indicative of ferruginous conditions (Poulton, 2021; Fig. 2). In the upper Fantasque Formation (10.0 to 14.3 m section height), pyrite framboids reappear and decrease in size up-section. Between 10 and 13 m, relatively large mean framboid diameters (6.8 to 9.6 μm) and modest trace metal enrichment suggest a return to predominantly dysoxic conditions. In the uppermost Fantasque Formation (13.0 to 14.3 m), populations of smaller framboids (mean diameters 5.7 to 6.5 μm) and iron speciation results [$Fe_{HR}/Fe_T < 0.38$; (Fe_{ox} + Fe_{py})/$Fe_{HR} < 0.8$] point to fluctuating dysoxic to episodically anoxic, ferruginous conditions immediately preceding the P-T transition.

In the lower Grayling Formation of Ursula Creek, the majority of samples lack pyrite framboids, defining a short-lived Early Triassic "framboid gap", a phenomenon observed elsewhere and linked to ferruginous conditions or reoxygenation (e.g., Yang et al., 2024). At Ursula Creek, evaluated Fe_{HR}/Fe_T values (> 0.38) during this gap suggest the presence of anoxic conditions. While Fe_{py} concentrations are near zero, (Fe_{ox} + Fe_{py})/Fe_{HR} values are generally beyond 0.8. These iron data, combined with trace metal enrichments and Mo_{EF}/U_{EF} values ranging from 0.1 to 1.0 × seawater, indicate that ferruginous conditions (oxygen-depleted and sulfide-free) prevailed in the earliest Triassic at Ursula Creek, punctuated by brief episodes of dysoxia (Fig. 2).

Previous work on the Chibi section has shown that the Upper Permian Talung Formation accumulated in predominantly dysoxic settings with intermittent anoxic/euxinic episodes, as indicated by abundant siliceous sponge spicules and radiolarians, rare calcareous benthic fossils, and pyrite framboid distributions (Yang et al., 2022; Fig. 5). In this study, our new iron speciation data and Mo-U covariations further confirm this dynamic redox framework. Most samples exhibit Mo_{EF}/U_{EF} ratios between 0.1 and 1 × seawater, suggesting predominantly dysoxic to anoxic conditions, whereas a few samples show Mo_{EF}/U_{EF} ratios > 1 × seawater, indicative of intermittent euxinic conditions (Fig. 5). Elevated Fe_{HR}/Fe_T values, coupled with comparatively low Fe_{py}/Fe_T values and Mo_{EF}/U_{EF} ratios < 1 × seawater, further suggest episodically ferruginous conditions (Fig. 5). SEM observation found that framboids at Chibi are well-preserved (Fig. 4C), showing convincing result of Fe proxies. Although the Lower Daye Formation (0 to 2.7 m section height) lacks pyrite framboids, other redox indicators including the presence of laminated, fossil-poor facies, evaluated Fe_{HR}, and pyrite depletion collectively suggest the development of Fe(II)-rich, oxygen-limited environments during the framboid gap interval

(Yang et al., 2022; Müller et al., 2023; Fig. 5). The reoccurrence of populations of small framboids (mean diameters 5.6 to 7.2 μm) together with our iron speciation constraints, suggests that ferruginous settings persisted into the earliest Triassic (Yang et al., 2022; Fig. 5). Additionally, declined Mo_{EF}/U_{EF} ratios (< 0.1 × seawater) also suggest weak Mo enrichment under oxygen-restricted but non-euxinic conditions during this interval (Figs. 5 and 6B). Overall, the Daye Formation at the Chibi section records predominantly ferruginous depositional conditions.

5.2 P-T oceanic redox variation: causes and consequences

To investigate global redox evolution across the P-T transition, we compiled iron speciation records from slope to basinal sections across Panthalassa, Tethys and the northwestern margin of Pangaea (Figs. 7 and 8). The P-T transition in each section is defined by the initial occurrence of the conodont species *Hindeodus parvus* or, alternatively, the minimum value of the well-known first major P-T negative carbon isotopic excursion (e.g., Yuan et al., 2014; Yang et al., 2022).

The Waiheke section of New Zealand provides one of the few available records from Panthalassa. Iron speciation and trace elements indicate fluctuating ferruginous and euxinic conditions during the P-T crisis. The elevated Fe_{HR} but low Fe_{py} and Mo/Al collectively suggest ferruginous conditions occurred during the upper Changhsingian in this area (Grasby et al., 2021; Takahashi et al., 2021; Fig. 7). In bedded cherts of the P-T transition, high Fe_{HR}/Fe_T and U/Al ratios, coupled with strong pyritization and elevated Mo/Al values, indicate the presence of euxinic settings (Takahashi et al., 2021; Fig. 7). Two distinct intervals characterized by evaluated Fe_{HR}/Fe_T, low Fe_{py}/Fe_{HR} and Mo/Al values are suggestive of recurring ferruginous episodes during the P-T transition. In contrast, low Fe_{HR}/Fe_T values (< 0.22) during the earliest Triassic suggest episodes of reoxygenation (Takahashi et al., 2021; Fig. 7).

Stratigraphic records from the northern marginal slopes and basins of South China consistently document a transition from dysoxic/euxinic to ferruginous settings from the Late Permian to Early Triassic (Cao et al., 2009; Xiang et al., 2020; Yang et al., 2024; Fig. 8). The Meishan GSSP section offers a particularly well-resolved example. There, evidence of green sulfur bacteria based on biomarkers suggests that euxinic conditions were widespread during the latest Permian (Cao et al., 2009). Several samples from the upper Changhsingian part exhibit evaluated Fe_{HR}/Fe_T (> 0.38) and reduced Fe_{py}/Fe_{HR} values (< 0.6), indicating episodic ferruginous conditions (Xiang et al., 2020). In the earliest Triassic, a marked decline in Fe_{py}/Fe_{HR} values further supports stable ferruginous conditions at Meishan (Xiang et

al., 2020; Fig. 7). This redox pattern is corroborated by iron speciation data from multiple well-documented sections including Ganxi, Xibeixiang, Chibi, Xiakou, Shangsi and Ruichang, which collectively support the development of regionally extensive ferruginous states in the earliest Triassic with episodic intervals of reoxygenation (Shen et al., 2016; Lei et al., 2017; Xiang et al., 2016; Ge et al., 2022; Yang et al., 2024; Figs. 7 and 8c).

Iron speciation constraints from the Arabian Margin (Oman and the United Arab Emirates) in western Neo-Tethys, and from the Xiang-Qian-Gui Basin of South China, similarly point to iron-rich, oxygen-depleted marine environments prevailing from the end of the Permian into the earliest Triassic, interrupted by short-lived oxygenation pulses during the Changhsingian (Clarkson et al., 2016; Xiang et al., 2022; Yang et al., 2024).

The redox evolution along the northwestern margin of Pangaea exhibits significant spatial heterogeneity. The Ursula Creek section records a transition from dysoxic conditions in the Changhsingian to ferruginous conditions in the Griesbachian. In contrast, sections in Spitsbergen (Festningen, Deltadalen) and Greenland (Fiskegrav) document an opposing trend: a shift from ferruginous conditions to euxinia (Bond and Wignall, 2010; Mettam et al., 2017; Schobben et al., 2020; Fig. 7).

These compiled records reveal a spatially heterogeneous and temporally dynamic global redox landscape across the P-T transition. During the latest Permian, ferruginous conditions intermittently developed across different ocean basins. In the earliest Triassic, however, ferruginous conditions expanded significantly, particularly within Tethys. This expansion may have been driven by a combination of processes: 1) extensive deposition of Upper Permian evaporites and intensified anoxia accompanied by enhanced pyrite burial drew down the oceanic sulphate reservoir (Luo et al., 2010; Warren, 2010); 2) strong ocean stratification and sluggish circulation suppressed nutrient upwelling and marine primary productivity, thereby reducing organic-carbon fluxes and limiting microbial sulphate reduction (e.g., Song et al., 2014; Clarkson et al., 2016; Sun, 2024); and 3) intense weathering of Fe-bearing silicate minerals under the Early Triassic extreme greenhouse delivered abundant Fe_{HR} to the oceans, resulting in a marked rise in Fe_{HR} input over sulphate (e.g., Poulton and Canfield, 2011).

The widespread development of ferruginous conditions in the Early Triassic may have significantly impacted nutrient dynamics, with phosphorus (P) cycling being a key mediator—consistent with

observations from past oceanic anoxic events (Papadomanolaki et al., 2022). Enhanced chemical weathering on land in the aftermath of the P-T transition likely boosted detrital delivery to the oceans (Sheldon, 2006; Algeo and Twitchett, 2010; Sun et al., 2018). However, despite the enhanced detrital delivery, marine primary productivity did not increase globally during the P-T transition; instead, it exhibited strong regional heterogeneity (e.g., Algeo et al., 2013; Grasby et al., 2016, 2020; Müller et al., 2022; Zhang et al., 2023; Sun, 2024). In South China, primary productivity underwent a catastrophic collapse across the EPME, as indicated by sharp declines in total organic carbon concentrations and organic carbon accumulation rates, together with evidence for restricted P recycling and negative cadmium isotopic excursions, while productivity in other Tethyan regions remained relatively stable or showed only modest increases (Algeo et al., 2013; Schobben et al., 2015; Shen et al., 2015; Müller et al., 2022; Zhang et al., 2023). Some sections from the northwestern margin of Pangaea and deep-water Panthalassic settings record substantial increases in organic carbon fluxes and marine productivity during the Early Triassic (Algeo et al., 2013; Schobben et al., 2020). In the study area, indicators from the phosphorus cycle and trace elements document a reduction in primary productivity (Müller et al., 2022; Woods et al., 2023). The contradiction between enhanced continental weathering and reduced marine primary productivity likely reflects multiple environmental stresses during the P-T transition, including reduced vertical mixing and nutrient upwelling due to strong thermal stratification, disrupted nutrient recycling, intensified redox instability, and extreme temperature stress on marine ecosystems and primary producers (e.g., Grasby et al., 2016; Ge and Bond, 2022; Knies et al., 2022). The observed covariation between redox conditions and primary productivity across the P-T transition—where productivity was lower under ferruginous conditions and higher under euxinic conditions—suggests that the widespread ferruginous conditions in the Early Triassic further support the redox constraint on primary production (e.g., Schobben et al., 2020; Müller et al., 2022; Ge et al., 2022; Woods et al., 2023). Ferruginous conditions could have promoted the sequestration of P into authigenic Fe(II)-bearing minerals such as vivianite, as well as through incorporation into green-rust phases and co-precipitation with iron oxides (Bjerrum and Canfield, 2002; Zegeye et al., 2012; Xiong et al., 2019). Such enhanced P retention in sediments would have reduced the return flux of recycled P to the water column, potentially weakening the positive feedback between P recycling, primary productivity, and anoxia in ancient ferruginous marine systems. Therefore, oxygen depletion, together with the potential linkage between ferruginous

conditions and nutrient limitation, may have played a key role in triggering the EPME and delaying the recovery.

6 Conclusions

Permian-Triassic records from the equatorial eastern Tethys (Chibi, South China) and the northwestern margin of Pangaea (Ursula Creek, western Canada) document distinct redox evolutions across this major transition in Earth history. A multi-proxy approach integrating pyrite framboid size distributions, Mo-U covariation, and iron speciation indicates that bottom waters at both locations were predominantly dysoxic during the Late Permian. In the Early Triassic, however, the Ursula Creek section records a marked intensification of oxygen depletion, as reflected by smaller pyrite framboid sizes and stronger Mo and U enrichments, together with enrichment of Fe_{HR} and limited pyritization of Fe_{HR}, indicating the development of predominantly ferruginous anoxic conditions. Although the Chibi section exhibits weaker Mo and U enrichments, iron speciation signatures suggest that bottom waters were under oxygen-depleted ferruginous conditions. The transition from predominantly dysoxic conditions in the Late Permian to ferruginous conditions in the Early Triassic in epicontinental seas suggests that marine ecosystem collapse during the EPME may have been linked to combined oxygen and nutrient stress under expanding ferruginous conditions.

Author contributions

All authors have been involved in the present work, have approved the manuscript, and agree to its submission. Fen Yang designed this study. Fen Yang, Yadong Sun, Stephen E. Grasby and David P.G. Bond collected the samples used in this study. Fen Yang completed the data preparation and analysis with the help of Sen Li. The manuscript was mainly written by Fen Yang and Sen Li with contributions from all authors. Sen Li is designated as the main corresponding author: lisen@cug.edu.cn.

Competing interests

The authors confirm that there are no financial or personal affiliations that could be perceived as influencing the results presented in this study.

Financial support

This work was jointly supported by the National Natural Science Foundation of China (Grant No. 42272022), the Guangxi Natural Science Foundation (No. 2026GXNSFBA00640099), the China Postdoctoral Science Foundation (grants No. 2025M770406), the geological survey projects of the China Geological Survey (Grants DD202501029, DD20242650). DPGB acknowledges NERC Grant NE/V001639/1.

References

Alcott, L. J., Krause, A. J., Hammarlund, E. U., Bjerrum, C. J., Scholz, F., Xiong, Y., Hobson, A. J., Neve, L., Mills, B. J. W., März, C., Schnetger, B., Bekker, A. and Poulton, S. W.: Development of Iron Speciation Reference Materials for Palaeoredox Analysis, Geostand. Geoanal. Res., 44, 581–591, https://doi.org/10.1111/ggr.12342, 2020.

Algeo, T. J. and Ingall, E.: Sedimentary Corg : P ratios, paleocean ventilation, and Phanerozoic atmospheric pO_2, Palaeogeogr. Palaeoclimatol. Palaeoecol., 256, 130–155, https://doi.org/10.1016/j.palaeo.2007.02.029, 2007.

Algeo, T. J., Ellwood, B., Nguyen, T. K. T., Rowe, H. and Maynard, J. B.: The Permian–Triassic boundary at Nhi Tao, Vietnam: evidence for recurrent influx of sulfidic watermasses to a shallow-marine carbonate platform, Palaeogeogr. Palaeoclimatol. Palaeoecol., 252(1–2), 304–327, https://doi.org/10.1016/j.palaeo.2006.11.055, 2007.

Algeo, T., Shen, Y., Zhang, T., Lyons, T., Bates, S., Rowe, H. and Nguyen, T.K.T.: Association of ^{34}S-depleted pyrite layers with negative carbonate $\delta^{13}C$ excursions at the Permian-Triassic boundary: Evidence for upwelling of sulfidic deep-ocean water masses, Geochem. Geophys. Geosyst., 9(4), https://doi.org/10.1029/2007GC001823, 2008.

Algeo, T. J. and Li, C.: Redox classification and calibration of redox thresholds in sedimentary systems, Geochim. Cosmochim. Acta., 287, 8–26, https://doi.org/10.1016/j.gca.2020.01.055, 2020.

Algeo, T. J. and Tribovillard, N.: Environmental analysis of paleoceanographic systems based on molybdenum–uranium covariation, Chem. Geol., 268, 211–225, https://doi.org/10.1016/j.chemgeo.2009.09.001, 2009.

Algeo, T. J. and Twitchett, R. J.: Anomalous Early Triassic sediment fluxes due to elevated weathering

453 rates and their biological consequences, Geology, 38, 1023–1026, https://doi.org/10.1130/G31203.1,
454 2010.
455 Algeo, T. J., Henderson, C. M., Tong, J., Feng, Q., Yin, H. and Tyson, R. V.: Plankton and productivity
456 during the Permian–Triassic boundary crisis: an analysis of organic carbon fluxes. Glob. Planet. Change,
457 105, 52–67, https://doi.org/10.1016/j.gloplacha.2012.02.008, 2013.
458 Algeo, T. J., Hinnov, L., Moser, J., Maynard, J. B., Elswick, E., Kuwahara, K. and Sano, H.: Changes in
459 productivity and redox conditions in the Panthalassic Ocean during the latest Permian, Geology, 38, 187–
460 190, https://doi.org/10.1130/G30483.1, 2010.
461 Algeo, T. J., Kuwahara, K., Sano, H., Bates, S., Lyons, T., Elswick, E., Hinnov, L., Ellwood, B., Moser,
462 J. and Maynard, J. B.: Spatial variation in sediment fluxes, redox conditions, and productivity in the
463 Permian–Triassic Panthalassic Ocean, Palaeogeogr. Palaeoclimatol. Palaeoecol., 308(1-2), 65–83,
464 https://doi.org/10.1016/j.palaeo.2010.07.007, 2011.
465 Beatty, T. W., Zonneveld, J. P. and Henderson, C. M.: Anomalously diverse Early Triassic ichnofossil
466 assemblages in northwest Pangea: A case for a shallow-marine habitable zone, Geology, 36, 771–774,
467 https://doi.org/10.1130/G24952A.1, 2008.
468 Bjerrum, C. J. and Canfield, D. E.: Ocean productivity before about 1.9 Gyr ago limited by phosphorus
469 adsorption onto iron oxides, Nature, 417, 159–162, https://doi.org/10.1038/417159a, 2002.
470 Bond, D. P. G. and Wignall, P. B.: Pyrite framboid study of marine Permian–Triassic boundary sections:
471 A complex anoxic event and its relationship to contemporaneous mass extinction, GSA Bulletin., 122,
472 1265–1279, https://doi.org/10.1130/B30042.1, 2010.
473 Burgess, S. D. and Bowring, S. A.: High-precision geochronology confirms voluminous magmatism
474 before, during, and after Earth's most severe extinction, Sci. Adv. 1, e1500470,
475 https://doi.org/10.1126/sciadv.1500470, 2015.
476 Canfield, D. E., Raiswell, R., Westrich, J. T., Reaves, C. M. and Berner, R. A.: The use of chromium
477 reduction in the analysis of reduced inorganic sulfur in sediments and shales, Chem. Geol., 54, 149–155,
478 https://doi.org/10.1016/0009-2541(86)90078-1, 1986.
479 Canfield, D. E., Poulton, S. W., Knoll, A. H., Narbonne, G. M., Ross, G., Goldberg, T. and Strauss, H.:
480 Ferruginous Conditions Dominated Later Neoproterozoic Deep-Water Chemistry, Science, 321, 949–952,
481 https://doi.org/10.1126/science.1154499, 2008.

Cao, C., Love, G. D., Hays, L. E., Wang, W., Shen, S. and Summons, R. E.: Biogeochemical evidence for euxinic oceans and ecological disturbance presaging the end-Permian mass extinction event, Earth Planet. Sci. Lett., 281, 188–201, https://doi.org/10.1016/j.epsl.2009.02.012, 2009.

Cawood, P. A., Zhao, G. C., Yao, J. L., Wang, W., Xu, Y. J. and Wang, Y. J.: Reconstructing South China in Phanerozoic and Precambrian supercontinents, Earth Sci. Rev. 186, 173–194, https://doi.org/10.1016/j.earscirev.2017.06.001, 2018.

Chen, J. T., Montañez, P. I., Qi, Y. P., Shen, S. Z. and Wang, X. D.: Strontium and carbon isotopic evidence for decoupling of pCO_2 from continental weathering at the apex of the late Paleozoic glaciation, Geology, 46 (5), 395–398, https://doi.org/10.1130/G40093.1, 2018.

Chen, Z. Q. and Benton, M. J.: The timing and pattern of biotic recovery following the end-Permian mass extinction, Nature Geosci., 5, 375–383, https://doi.org/10.1038/ngeo1475, 2012.

Chen, Z. Q., Fang, Y., Wignall, P. B., Guo, Z., Wu, S., Liu, Z., Wang, R., Huang, Y. and Feng, X.: Microbial Blooms Triggered Pyrite Framboid Enrichment and Oxygen Depletion in Carbonate Platforms Immediately After the Latest Permian Extinction, Geophys. Res. Lett., 49, e2021GL096998, https://doi.org/10.1029/2021GL096998, 2022.

Clarkson, M. O., Poulton, S. W., Guilbaud, R. and Wood, R. A.: Assessing the utility of Fe/Al and Fe-speciation to record water column redox conditions in carbonate-rich sediments, Chem. Geol., 382, 111–122, https://doi.org/10.1016/j.chemgeo.2014.05.031, 2014.

Clarkson, M. O., Wood, R. A., Poulton, S. W., Richoz, S., Newton, R. J., Kasemann, S. A., Bowyer, F. and Krystyn, L.: Dynamic anoxic ferruginous conditions during the end-Permian mass extinction and recovery, Nat Commun., 7, 12236, https://doi.org/10.1038/ncomms12236, 2016.

Crowell, J. C.: The Ending of the Late Paleozoic Ice Age During the Permian Period. In: Scholle, P.A., Peryt, T. M., Ulmer-Scholle, D. S. (eds) The Permian of Northern Pangea. Springer, Berlin, Heidelberg. https://doi.org/10.1007/978-3-642-78593-1_5, 1995.

Derry, L. A.: Causes and consequences of mid-Proterozoic anoxia, Geophys. Res. Lett., 42, 8538–8546, https://doi.org/10.1002/2015GL065333, 2015.

Erwin, D. H.: Extinction: How life on Earth nearly ended 250 million years ago, Princeton University Press, Princeton, NJ, US, viii, 296 pp., 2006.

Fan, J. X., Shen, S. Z., Erwin, D. H., Sadler, P. M., MacLeod, N., Cheng, Q. M., Hou, X. D., Yang, J.,

Wang, X. D., Wang, Y., Zhang, H., Chen, X., Li, G. X., Zhang, Y. C., Shi, Y. K., Yuan, D. X., Chen, Q., Zhang, L. N., Li, C. and Zhao, Y. Y.: A high-resolution summary of Cambrian to Early Triassic marine invertebrate biodiversity, Science, 367, 272–277, https://doi.org/10.1126/science.aax4953, 2020.

Feng, Z. Z., Yang, Y. Q., Jin, Z. K., He, Y. B., Wu, S. H., Xin, W. J., Bao, Z. D. and Tan, J.: Lithofacies paleogeography of the Permian of South China. Acta Sedimentol. Sin.14 (2), 1–11, 1996 (in Chinese with English abstract).

Foster, W. J. and Twitchett, R. J.: Functional diversity of marine ecosystems after the Late Permian mass extinction event, Nature Geosci., 7, 233–238, https://doi.org/10.1038/ngeo2079, 2014.

Frank, A. B., Karapunar, B., Grasby, S. E., Koşun, E., Lahajnar, N., Gómez Correa, M. A., Buchwald, S. Z., Metzke, M. and Foster, W. J.: Assessing the role of anoxia as a potential extinction driver in the shallow marine Neotethys during the Permian-Triassic mass extinction, Chem. Geol., 696, 123108, https://doi.org/10.1016/j.chemgeo.2025.123108, 2025.

Garbelli, C., Angiolini, L., Brand, U., Shen, S., Jadoul, F., Posenato, R., Azmy, K. and Cao, C.: Neotethys seawater chemistry and temperature at the dawn of the end Permian mass extinction, Gondwana Res., 35, 272–285, https://doi.org/10.1016/j.gr.2015.05.012, 2016.

Ge, X., Chen, D., Zhang, G., Huang, T., Liu, M. and El-Shafeiy, M.: Marine redox evolution and organic accumulation in an intrashelf basin, NE Sichuan Basin during the Late Permian, Mar. Pet. Geol., 140, 105633, https://doi.org/10.1016/j.marpetgeo.2022.105633, 2022.

Ge, Y. and Bond, D. P. G.: Two deep marine oxygenation events during the Permian-Triassic boundary interval in South China: Relationship with ocean circulation and marine primary productivity, Earth-sci. Rev., 234, 104220, https://doi.org/10.1016/j.earscirev.2022.104220, 2022.

Georgiev, S. V., Horner, T. J., Stein, H. J., Hannah, J. L., Bingen, B. and Rehkämper, M.: Cadmium-isotopic evidence for increasing primary productivity during the Late Permian anoxic event, Earth Planet. Sci. Lett., 410, 84–96, https://doi.org/10.1016/j.epsl.2014.11.010, 2015.

Grasby, S. E. and Beauchamp, B.: Intrabasin variability of the carbon-isotope record across the Permian–Triassic transition, Sverdrup Basin, Arctic Canada, Chem. Geol., 253, 141–150, https://doi.org/10.1016/j.chemgeo.2008.05.005, 2008.

Grasby, S. E., Beauchamp, B., Embry, A. and Sanei, H.: Recurrent Early Triassic ocean anoxia, Geology, 41, 175–178, https://doi.org/10.1130/G33599.1, 2013.

Grasby, S. E., Beauchamp, B. and Knies, J.: Early Triassic productivity crises delayed recovery from world's worst mass extinction, Geology, 44, 779–782, https://doi.org/10.1130/G38141.1, 2016.

Grasby, S. E., Knies, J., Beauchamp, B., Bond, D. P. G., Wignall, P. and Sun, Y.: Global warming leads to Early Triassic nutrient stress across northern Pangea, GSA Bulletin., 132, 943–954, https://doi.org/10.1130/B32036.1, 2019.

Grasby, S. E., Bond, D. P. G., Wignall, P. B., Yin, R., Strachan, L. J. and Takahashi, S.: Transient Permian-Triassic euxinia in the southern Panthalassa deep ocean, Geology, 49, 889–893, https://doi.org/10.1130/G48928.1, 2021.

Grice, K., Cao, C., Love, G. D., Böttcher, M. E., Twitchett, R. J., Grosjean, E., Summons, R. E., Turgeon, S. C., Dunning, W. and Jin, Y.: Photic Zone Euxinia During the Permian-Triassic Superanoxic Event, Science, 307, 706–709, https://doi.org/10.1126/science.1104323, 2005.

He, B., Xu, Y. G., Huang, X. L., Luo, Z. Y., Shi, Y. R., Yang, Q. J. and Yu, S. Y.: Age and duration of the Emeishan flood volcanism, SW China: Geochemistry and SHRIMP zircon U-Pb dating of silicic ignimbrites, post-volcanic Xuanwei Formation and clay tuff at the Chaotian section, Earth Planet. Sci. Lett. 255, 306–323, https://doi.org/10.1016/j.epsl.2006.12.021, 2007.

Henderson, C. M.: Uppermost Permian conodonts and the Permian-Triassic boundary in the Western Canada Sedimentary Basin, Bulletin of Canadian Petroleum Geology, 45, 693–707, https://doi.org/10.35767/gscpgbull.45.4.693, 1997.

Hotinski, R. M., Bice, K. L., Kump, L. R., Najjar, R. G. and Arthur, M. A.: Ocean stagnation and end-Permian anoxia, Geology, 29, 7–10, https://doi.org/10.1130/0091-7613(2001)029<0007:OSAEPA>2.0.CO;2, 2001.

Hülse, D., Lau, K.V., van de Velde, S. J., Arndt, S., Meyer, K. M. and Ridgwell, A.: End-Permian marine extinction due to temperature-driven nutrient recycling and euxinia, Nat. Geosci., 14, 862–867, https://doi.org/10.1038/s41561-021-00829-7, 2021.

Isozaki, Y.: Permo-Triassic Boundary Superanoxia and Stratified Superocean: Records from Lost Deep Sea, Science, 276, 235–238, https://doi.org/10.1126/science.276.5310.235, 1997.

Isozaki, Y.: Integrated "plume winter" scenario for the double-phased extinction during the Paleozoic–Mesozoic transition: The G-LB and P-TB events from a Panthalassan perspective, J. Asian earth sci., 36, 459–480, https://doi.org/10.1016/j.jseaes.2009.05.006, 2009.

569 Joachimski, M. M., Lai, X., Shen, S., Jiang, H., Luo, G., Chen, B., Chen, J. and Sun, Y.: Climate warming
570 in the latest Permian and the Permian–Triassic mass extinction, Geology, 40, 195–198,
571 https://doi.org/10.1130/G32707.1, 2012.
572 Knies, J., Schönenberger, J., Zwingmann, H., van der Lelij, R., Smelror, M., Vullum, P. E., Brönner, M.,
573 Vogt, C., Fredin, O., Müller, A., Grasby, S. E., Beauchamp, B. and Viola, G.: Continental weathering and
574 recovery from ocean nutrient stress during the Early Triassic Biotic Crisis, Commun Earth Environ, 3,
575 161, https://doi.org/10.1038/s43247-022-00480-z, 2022.
576 Knoll, A. H., Bambach, R. K., Canfield, D. E. and Grotzinger, J. P.: Comparative Earth History and Late
577 Permian Mass Extinction, Science, 273, 452–457, https://doi.org/10.1126/science.273.5274.452, 1996.
578 Kump, L. R., Pavlov, A., and Arthur, M. A.: Massive release of hydrogen sulfide to the surface ocean and
579 atmosphere during intervals of oceanic anoxia, Geology, 33, 397–400, https://doi.org/10.1130/G21295.1,
580 2005.
581 Lau, K. V., Maher, K., Altiner, D., Kelley, B. M., Kump, L. R., Lehrmann, D. J., Silva-Tamayo, J. C.,
582 Weaver, K. L., Yu, M. and Payne, J. L.: Marine anoxia and delayed Earth system recovery after the end-
583 Permian extinction, Proc. Natl. Acad. Sci., 113, 2360–2365, https://doi.org/10.1073/pnas.1515080113,
584 2016.
585 Lei, L. D., Shen, J., Li, C., Algeo, T. J., Chen, Z. Q., Feng, Q. L., Cheng, M., Jin, C. S. and Huang, J. H.:
586 Controls on regional marine redox evolution during Permian-Triassic transition in South China,
587 Palaeogeogr. Palaeoclimatol. Palaeoecol., 486, 17–32, https://doi.org/10.1016/j.palaeo.2017.02.010,
588 2017.
589 López-Gómez, J., Arche, A., Marzo, M. and Durand, M.: 2005. Stratigraphical and palaeogeographical
590 significance of the continental sedimentary transition across the Permian–Triassic boundary in Spain,
591 Palaeogeogr. Palaeoclimatol. Palaeoecol., 229, 3–23, https://doi.org/10.1016/j.palaeo.2004.11.028, 2005.
592 Luo, G., Kump, L. R., Wang, Y., Tong, J., Arthur, M. A., Yang, H., Huang, J., Yin, H. and Xie, S.: Isotopic
593 evidence for an anomalously low oceanic sulfate concentration following end-Permian mass extinction,
594 Earth Planet. Sci. Lett., 300, 101–111, https://doi.org/10.1016/j.epsl.2010.09.041, 2010.
595 Medici, G., West, L. J. and Mountney, N. P.: Sedimentary flow heterogeneities in the Triassic U.K.
596 Sherwood Sandstone Group: insights for hydrocarbon exploration, Geological Journal, 54(3), 1361–1378,
597 https://doi.org/10.1002/gj.3233, 2019.

598 Mettam, C., Zerkle, A. L., Claire, M. W., Izon, G., Junium, C. J. and Twitchett, R. J.: High-frequency
599 fluctuations in redox conditions during the latest Permian mass extinction, Paleogeogr. Paleoclimatol.
600 Paleoecol., 485, 210–223, https://doi.org/10.1016/j.palaeo.2017.06.014, 2017.
601 Meyer, K. M., Kump, L. R. and Ridgwell, A.: Biogeochemical controls on photic-zone euxinia during
602 the end-Permian mass extinction, Geology, 36, 747–750, https://doi.org/10.1130/G24618A.1, 2008.
603 Monger, J., Price, R.: The Canadian Cordillera: geology and tectonic evolution, GSEG Recorder27, 17–
604 36, 2002.
605 Müller, J., Sun, Y., Yang, F., Fantasia, A. and Joachimski, M.: Phosphorus Cycle and Primary Productivity
606 Changes in the Tethys Ocean During the Permian-Triassic Transition: Starving Marine Ecosystems, Front.
607 Earth Sci., 10, https://doi.org/10.3389/feart.2022.832308, 2022.
608 Müller, J., Sun, Y. D., Yang, F., Regelous, M. and Joachimski, M. M.: Manganous water column in the
609 Tethys Ocean during the Permian-Triassic transition, Glob. Planet. Change., 222, 104067,
610 https://doi.org/10.1016/j.gloplacha.2023.104067, 2023.
611 Newby, S. M., Owens, J. D., Schoepfer, S. D. and Algeo, T. J.: Transient ocean oxygenation at end-
612 Permian mass extinction onset shown by thallium isotopes, Nat. Geosci., 14, 678–683,
613 https://doi.org/10.1038/s41561-021-00802-4, 2021.
614 Nielsen, J. K., Shen, Y., Piasecki, S. and Stemmerik, L.: No abrupt change in redox condition caused the
615 end-Permian marine ecosystem collapse in the East Greenland Basin, Earth Planet. Sci. Lett., 291, 32–
616 38, https://doi.org/10.1016/j.epsl.2009.12.043, 2010.
617 Papadomanolaki, N. M., Lenstra, W. K., Wolthers, M. and Slomp, C. P.: Enhanced phosphorus recycling
618 during past oceanic anoxia amplified by low rates of apatite authigenesis, Sci. Adv., 8, eabn2370,
619 https://doi.org/10.1126/sciadv.abn2370, 2022.
620 Pietsch, C., Ritterbush, K. A., Thompson, J. R., Petsios, E. and Bottjer, D. J.: Evolutionary models in the
621 early Triassic marine realm, Palaeogeogr. Palaeoclimatol. Palaeoecol. 513, 65–85,
622 https://doi.org/10.1016/j.palaeo.2017.12.016, 2019.
623 Poulton, S. W.: The low-temperature geochemical cycle of iron: From continental fluxes to marine
624 sediment deposition, Am. J. Sci., 302, 774–805, https://doi.org/10.2475/ajs.302.9.774, 2002.
625 Poulton, S. W.: The Iron Speciation Paleoredox Proxy, Elements in Geochemical Tracers in Earth System
626 Science, https://doi.org/10.1017/9781108847148, 2021.

627 Poulton, S. W. and Canfield, D. E.: Development of a sequential extraction procedure for iron:
628 implications for iron partitioning in continentally derived particulates, Chem. Geol., 214, 209–221,
629 https://doi.org/10.1016/j.chemgeo.2004.09.003, 2005.
630 Poulton, S. W. and Canfield, D. E.: Ferruginous Conditions: A Dominant Feature of the Ocean through
631 Earth's History, Elements, 7, 107–112, https://doi.org/10.2113/gselements.7.2.107, 2011.
632 Proemse, B. C., Grasby, S. E., Wieser, M. E., Mayer, B. and Beauchamp, B.: Molybdenum isotopic
633 evidence for oxic marine conditions during the latest Permian extinction, Geology, 41, 967–970,
634 https://doi.org/10.1130/G34466.1, 2013.
635 Pruss, S. B., Bottjer, D. J., Corsetti, F. A. and Baud, A.: A global marine sedimentary response to the end-
636 Permian mass extinction: Examples from southern Turkey and the western United States, Earth-sci. Rev.,
637 78, 193–206, https://doi.org/10.1016/j.earscirev.2006.05.002, 2006.
638 Schobben, M., Foster, W. J., Sleveland, A. R. N., Zuchuat, V., Svensen, H. H., Planke, S., Bond, D. P. G.,
639 Marcelis, F., Newton, R. J., Wignall, P. B. and Poulton, S. W.: A nutrient control on marine anoxia during
640 the end-Permian mass extinction, Nat. Geosci., 13, 640–646, https://doi.org/10.1038/s41561-020-0622-
641 1, 2020.
642 Schobben, M., Stebbins, A., Ghaderi, A., Strauss, H., Korn, D. and Korte, C.: Flourishing ocean drives
643 the end-Permian marine mass extinction, Proc. Natl. Acad. Sci. U.S.A., 112(33), 10298–10303,
644 https://doi.org/10.1073/pnas.1503755112, 2015.
645 Schoepfer, S. D., Henderson, C. M., Garrison, G. H., Foriel, J., Ward, P. D., Selby, D., Hower, J. C.,
646 Algeo, T. J. and Shen, Y.: Termination of a continent-margin upwelling system at the Permian–Triassic
647 boundary (Opal Creek, Alberta, Canada), Glob. Planet. Change., 105, 21–35,
648 https://doi.org/10.1016/j.gloplacha.2012.07.005, 2013.
649 Scholz, F., McManus, J. and Sommer, S.: The manganese and iron shuttle in a modern euxinic basin and
650 implications for molybdenum cycling at euxinic ocean margins, Chem. Geol., 355, 56–68,
651 https://doi.org/10.1016/j.chemgeo.2013.07.006, 2013.
652 Scotese, C.: Atlas of Middle & Late Permian and Triassic Paleogeographic Maps, Scotese, C.R., 2014.
653 Atlas of Middle & Late Permian and Triassic Paleogeographic Maps, Maps 43–52, Volumes 3 & 4,
654 PALEOMAP PaleoAtlas for ArcGIS, PALEOMAP Project, Evanston, IL., 2014.
655 Sepkoski, J. J.: A Factor Analytic Description of the Phanerozoic Marine Fossil Record, Paleobiology, 7,

36–53, 1981.

Sheldon, N. D.: Abrupt chemical weathering increase across the Permian–Triassic boundary, Palaeogeogr. Palaeoclimatol. Palaeoecol., 231, 315–321, https://doi.org/10.1016/j.palaeo.2005.09.001, 2006.

Shen, J., Algeo, T. J., Hu, Q., Zhang, N., Zhou, L., Xia, W., Xie, S. and Feng, Q.: Negative C-isotope excursions at the Permian-Triassic boundary linked to volcanism, Geology, 40, 963–966, https://doi.org/10.1130/G33329.1, 2012.

Shen, J., Feng, Q., Algeo, T. J., Li, C., Planavsky, N. J., Zhou, L. and Zhang, M.: Two pulses of oceanic environmental disturbance during the Permian–Triassic boundary crisis, Earth Planet. Sci. Lett., 443, 139–152, https://doi.org/10.1016/j.epsl.2016.03.030, 2016.

Shen, Y., Farquhar, J., Zhang, H., Masterson, A., Zhang, T. and Wing, B. A.: Multiple S-isotopic evidence for episodic shoaling of anoxic water during Late Permian mass extinction, Nat Commun., 2, 210, https://doi.org/10.1038/ncomms1217, 2011.

Shen, J., Schoepfer, S. D., Feng, Q.L., Zhou, L., Yu, J. X., Song, H. Y., Wie, H. Y. and Algeo, T. J.: Marine productivity changes during the end-Permian crisis and Early Triassic recovery, Earth-Sci. Rev., 149, 136–162, https://doi.org/10.1016/j.earscirev.2014.11.002, 2015.

Song, H., Tong, J., Algeo, T. J., Song, H., Qiu, H., Zhu, Y., Tian, L., Bates, S., Lyons, T. W., Luo, G. and Kump, L. R.: Early Triassic seawater sulfate drawdown, Geochim. Cosmochim. Acta., 128, 95–113, https://doi.org/10.1016/j.gca.2013.12.009, 2014.

Sperling, E. A., Wolock, C. J., Morgan, A. S., Gill, B. C., Kunzmann, M., Halverson, G. P., Macdonald, F. A., Knoll, A. H. and Johnston, D. T.: Statistical analysis of iron geochemical data suggests limited late Proterozoic oxygenation, Nature, 523, 451–454, https://doi.org/10.1038/nature14589, 2015.

Stebbins, A., Williams, J., Brookfield, M., Nye, S. W. and Hannigan, R.: Frequent euxinia in southern Neo-Tethys Ocean prior to the end-Permian biocrisis: Evidence from the Spiti region, India, Palaeogeogr. Palaeoclimatol. Palaeoecol., 516, 1–10, https://doi.org/10.1016/j.palaeo.2018.11.030, 2019.

Sun, H., Xiao, Y., Gao, Y., Zhang, G., Casey, J. F. and Shen, Y.: Rapid enhancement of chemical weathering recorded by extremely light seawater lithium isotopes at the Permian–Triassic boundary, Proc. Natl. Acad. Sci., 115, 3782–3787, https://doi.org/10.1073/pnas.1711862115, 2018.

Sun, Y.: Dynamics of nutrient cycles in the Permian–Triassic oceans, Earth-Sci. Rev., 258, 104914, https://doi.org/10.1016/j.earscirev.2024.104914, 2024.

Sun, Y., Joachimski, M. M., Wignall, P. B., Yan, C., Chen, Y., Jiang, H., Wang, L. and Lai, X.: Lethally Hot Temperatures During the Early Triassic Greenhouse, Science, 338, 366–370, https://doi.org/10.1126/science.1224126, 2012.

Takahashi, S., Hori, R. S., Yamakita, S., Aita, Y., Takemura, A., Ikehara, M., Xiong, Y., Poulton, S. W., Wignall, P. B., Itai, T., Campbell, H. J. and Spörli, B. K.: Progressive development of ocean anoxia in the end-Permian pelagic Panthalassa, Glob. Planet. Change., 207, 103650, https://doi.org/10.1016/j.gloplacha.2021.103650, 2021.

Taniwaki, T., Elders, C., Böttcher, M. E., Holman, A. I. and Grice, K.: Photic zone redox oscillations and microbialite development recorded by Early Triassic sediments of the Perth Basin: A geochemical approach, Geochim. Cosmochim. Acta., 336, 188–207, https://doi.org/10.1016/j.gca.2022.09.011, 2022.

Taylor, S. and McLennan, S.: The Continental Crust: Its Composition and Evolution, Department of Geosciences Faculty Publications, 1985.

Tribovillard, N., Algeo, T. J., Lyons, T. and Riboulleau, A.: Trace metals as paleoredox and paleoproductivity proxies: An update, Chem. Geol., 232, 12–32, https://doi.org/10.1016/j.chemgeo.2006.02.012, 2006.

Tribovillard, N., Algeo, T. J., Baudin, F. and Riboulleau, A.: Analysis of marine environmental conditions based onmolybdenum–uranium covariation—Applications to Mesozoic paleoceanography, Chem. Geol., 324–325, 46–58, https://doi.org/10.1016/j.chemgeo.2011.09.009, 2012.

Wan, T.F.: The Tectonics of China: Data, Maps and Evolution, Springer-Verlag, Berlin, Heidelberg, 2012.

Wang, Y., Qian, X., Cawood, P. A., Liu, H., Feng, Q., Zhao, G., Zhang, Y., He, H., Zhang, P.: Closure of the East Paleotethyan Ocean and amalgamation of the Eastern Cimmerian and Southeast Asia continental fragments, Earth-Sci. Rev.186, 195–230, https://doi.org/10.1016/j.earscirev.2017.09.013, 2018.

Warren, J. K.: Evaporites through time: Tectonic, climatic and eustatic controls in marine and nonmarine deposits, Earth Sci. Rev., 98, 217–268, https://doi.org/10.1016/j.earscirev.2009.11.004, 2010.

Wignall, P. and Twitchett, R.: Extent, duration, and nature of the Permian-Triassic superanoxic event, in: Catastrophic events and mass extinctions: impacts and beyond, vol. Special Paper 356, edited by: Koeberl, C. and MacLoed, K., Geological Society of America, 395–413, 2002.

Wignall, P. B. and Hallam, A.: Anoxia as a cause of the Permian/Triassic mass extinction: facies evidence from northern Italy and the western United States, Palaeogeogr. Palaeoclimatol. Palaeoecol., 93, 21–46,

https://doi.org/10.1016/0031-0182(92)90182-5, 1992.

Wignall, P. B. and Newton, R.: Contrasting Deep-Water Records from the Upper Permian and Lower Triassic of South Tibet and British Columbia: Evidence for a Diachronous Mass Extinction, Palaios, 18, 153–167, 2003.

Wignall, P. B. and Twitchett, R. J.: Oceanic Anoxia and the End Permian Mass Extinction, Science, 272, 1155–1158, https://doi.org/10.1126/science.272.5265.1155, 1996.

Wilkin, R. T. and Barnes, H. L.: Pyrite formation by reactions of iron monosulfides with dissolved inorganic and organic sulfur species, Geochim. Cosmochim. Acta., 60, 4167–4179, https://doi.org/10.1016/S0016-7037(97)81466-4, 1996.

Wilkin, R. T., Barnes, H. L. and Brantley, S. L.: The size distribution of framboidal pyrite in modern sediments: An indicator of redox conditions, Geochim. Cosmochim. Acta., 60, 3897–3912, https://doi.org/10.1016/0016-7037(96)00209-8, 1996.

Winguth, C. and Winguth, A. M.: Simulating Permian–Triassic oceanic anoxia distribution: Implications for species extinction and recovery, Geology, 40(2), 127–130, https://doi.org/ 10.1130/g32453.1, 2012.

Woods, A. D., Zonneveld, J. P. and Wakefield, R.: Hyperthermal-driven anoxia and reduced productivity in the aftermath of the Permian-Triassic mass extinction: a case study from Western Canada, Front. Earth Sci., 11, https://doi.org/10.3389/feart.2023.1323413, 2023.

Wu, Y., Pohl, A., Tian, L., Corso, J. D., Cui, Y., Chu, D., Tong, J., Song, H., Song, H. and Song, H.: Recurrent marine anoxia in the Paleo-Tethys linked to constriction of seaways during the Early Triassic, Earth Planet. Sci. Lett., 643, 118882, https://doi.org/10.1016/j.epsl.2024.118882, 2024.

Xiang, L., Schoepfer, S. D., Zhang, H., Yuan, D., Cao, C., Zheng, Q., Henderson, C. M. and Shen, S.: Oceanic redox evolution across the end-Permian mass extinction at Shangsi, South China, Paleogeogr. Paleoclimatol. Paleoecol. 448, 59–71, https://doi.org/10.1016/j.palaeo.2015.10.046, 2016.

Xiang, L., Zhang, H., Schoepfer, S. D., Cao, C., Zheng, Q., Yuan, D., Cai, Y. and Shen, S.: Oceanic redox evolution around the end-Permian mass extinction at Meishan, South China, Paleogeogr. Paleoclimatol. Paleoecol., 544, 109626, https://doi.org/10.1016/j.palaeo.2020.109626, 2020.

Xiang, L., Schoepfer, S. D., Yuan, D. X., Zheng, Q. F. and Zhang, H.: Oceanic redox evolution across the end-Permian mass extinction at Penglaitan section, South China, Palaeoworld, 31, 93–102, https://doi.org/10.1016/j.palwor.2021.02.003, 2022.

Xiong, Y., Guilbaud, R., Peacock, C. L., Cox, R. P., Canfield, D. E., Krom, M. D. and Poulton, S. W.: Phosphorus cycling in Lake Cadagno, Switzerland: A low sulfate euxinic ocean analogue, Geochim. Cosmochim. Acta., 251, 116–135, https://doi.org/10.1016/j.gca.2019.02.011, 2019.

Yang, F., Sun, Y. D., Frings, P. J., Luo, L., E, J. W., Wang, L. N., Huang, Y. F., Wang, T., Müller, J. and Xie, S. C.: Collapse of Late Permian chert factories in the equatorial Tethys and the nature of the Early Triassic chert gap, Earth Planet. Sci. Lett., 600, 117861, https://doi.org/10.1016/j.epsl.2022.117861, 2022.

Yang, F., Li, S., An, K.Y., Bond, P.G.D., Ao, R., Wu, X.B., Ma, L.L. and Sun, Y.D.: 2024. Re-Evaluating Water Column Reoxygenation During the End Permian Mass Extinction. Geochem. Geophys. Geosyst. 25, https://doi.org/10.1029/2024gc011779, 2024.

Yuan, D., Shen, S., Henderson, C. M., Chen, J., Zhang, H. and Feng, H.: Revised conodont-based integrated high-resolution timescale for the Changhsingian Stage and end-Permian extinction interval at the Meishan sections, South China, Lithos, 204, 220–245, https://doi.org/10.1016/j.lithos.2014.03.026, 2014.

Zegeye, A., Bonneville, S., Benning, L. G., Sturm, A., Fowle, D. A., Jones, C., Canfield, D. E., Ruby, C., MacLean, L. C., Nomosatryo, S., Crowe, S. A. and Poulton, S. W.: Green rust formation controls nutrient availability in a ferruginous water column, Geology, 40, 599–602, https://doi.org/10.1130/G32959.1, 2012.

Zhang, G., Zhang, X., Hu, D., Li, D., Algeo, T. J., Farquhar, J., Henderson, C. M., Qin, L., Shen, M., Shen, D., Schoepfer, S. D., Chen, K. and Shen, Y.: Redox chemistry changes in the Panthalassic Ocean linked to the end-Permian mass extinction and delayed Early Triassic biotic recovery, Proc. Natl. Acad. Sci. U.S.A., 114, 1806–1810, https://doi.org/10.1073/pnas.1610931114, 2017.

Zhang, Y. X., Wen, H. J., Fan, H. F., Zhu, C. W., Xiao, J. F. and Qiao, P.: Cadmium isotopic evidence for reduced deep-water marine primary productivity during the end-Permian mass extinction, Earth Planet. Sci. Lett., 621, https://doi.org/10.1016/j.epsl.2023.118371, 2023.

Zhang, M., Qin, H., Hou, Y., He, K., Deng, C., Shen, S. Z. and Pan, Y. X.: Shifts in magnetic mineral assemblages support ocean deoxygenation before the end-Permian mass extinction, Commun. Earth Environ, 5, 218, https://doi.org/10.1038/s43247-024-01394-8, 2024.

Zelt, C. A., Ellis, R.M. and Zelt, B. C.: Three-dimensional structure across the Tintina strike-slip fault, northern Canadian Cordillera, from seismic refraction and reflection tomography, Geophys. J. Int. 167,

772 1292–1308, https://doi.org/10.1111/j.1365-246X.2006.03090.x, 2006.

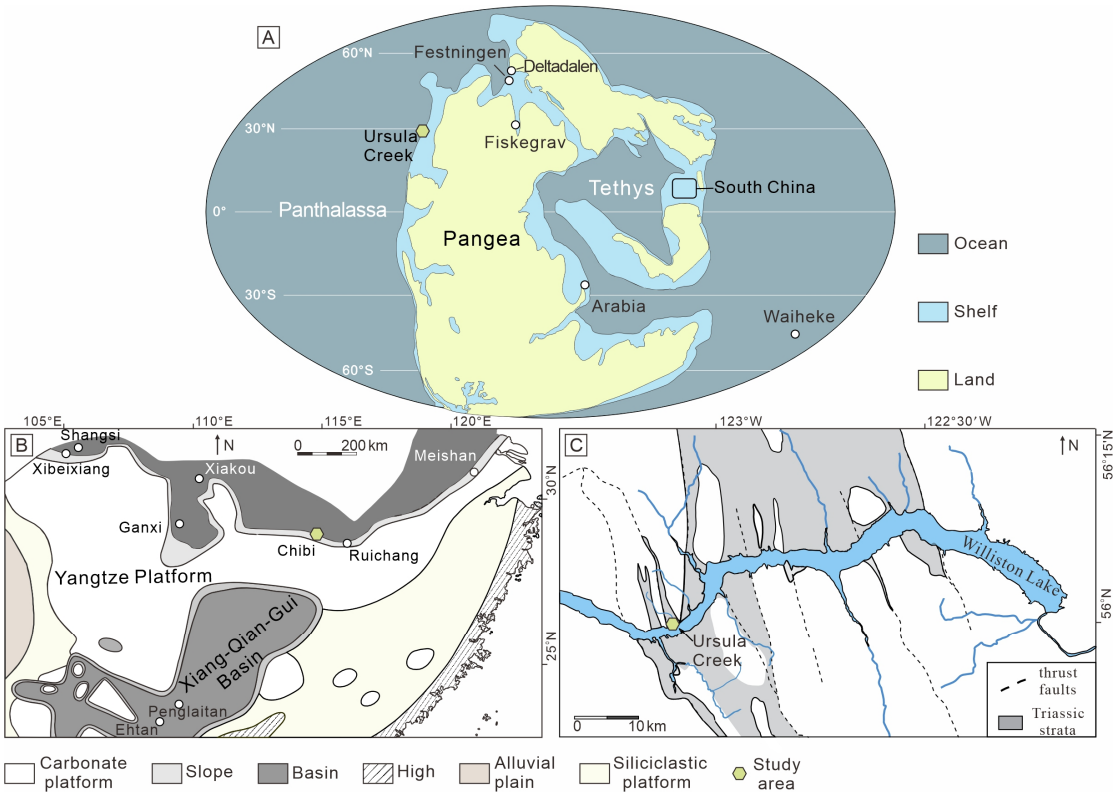

774 Figure 1. (A) Palaeogeographic reconstruction of Pangaea in the Late Permian (modified from Scotese,
775 2014). (B) Palaeogeographic reconstruction of the South China Craton during the Changhsingian
776 (modified from Feng et al., 1996). (C) Locations of the Ursula Creek section (modified from Wignall
777 and Newton, 2003).

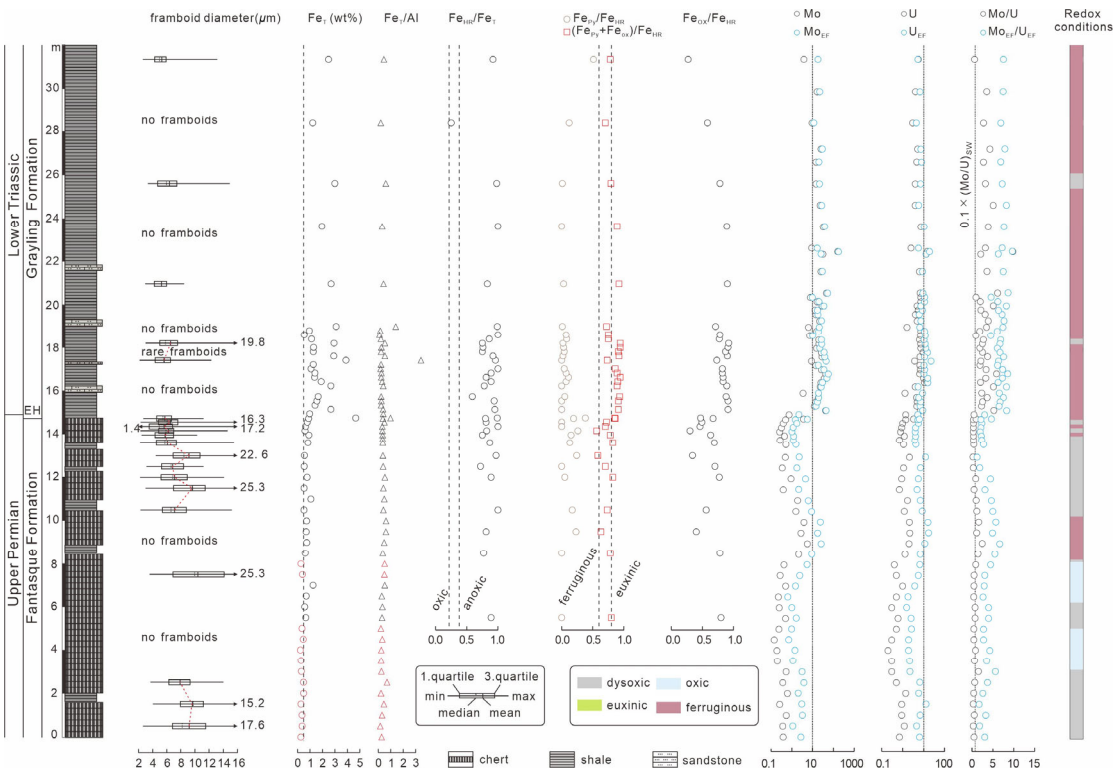

778

779 Figure 2. Stratigraphic log of the Ursula Creek section with total iron (Fe_T), Fe_T/Al, iron proxies
780 [Fe_{HR}/Fe_T, Fe_{Py}/Fe_{HR}, $(Fe_{Py}+Fe_{ox})/Fe_{HR}$, Fe_{ox}/Fe_{HR}], Mo and U concentrations, enrichment factors (Mo_{EF},
781 U_{EF}) and their ratios (Mo/U, Mo_{EF}/U_{EF}), and pyrite framboid "box-and-whisker" plots. The "box"
782 represents the interquartile range (25th–75th percentiles) of framboid diameters, the "whiskers" show the
783 minimum and maximum values, and the central lines mark the median and the mean.

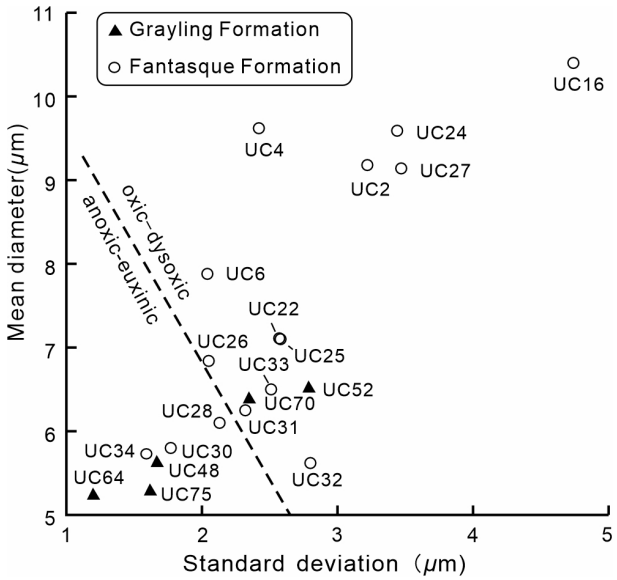

784

Figure 3. Mean diameter versus standard deviation of framboid size distributions for the Ursula Creek samples. The dashed line separates anoxic-euxinic from oxic-dysoxic conditions (cf. Wilkin et al., 1996).

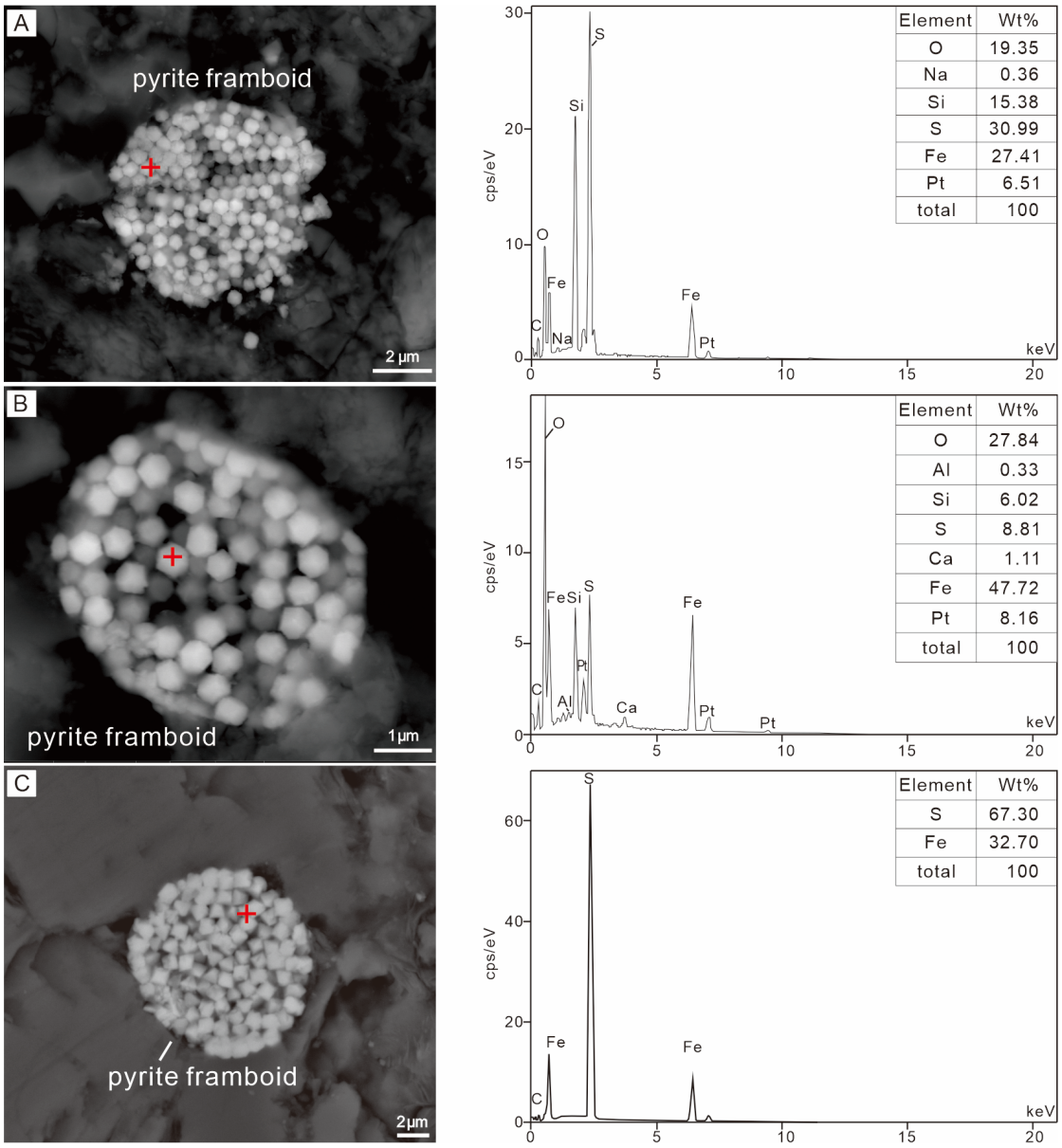

Figure 4. Mineral composition of pyrite framboids in samples from the Ursula Creek and Chibi sections. (A) SEM image and EDS spectrum at the red cross of a pyrite framboid from the lower Fantasque Formation, Ursula Creek; (B) SEM image and EDS spectrum at the red cross of a pyrite framboid from the lower Grayling Formation, Ursula Creek; and (C) SEM image and EDS spectrum at the red cross of a pyrite framboid from the lower Talung Formation, Chibi.

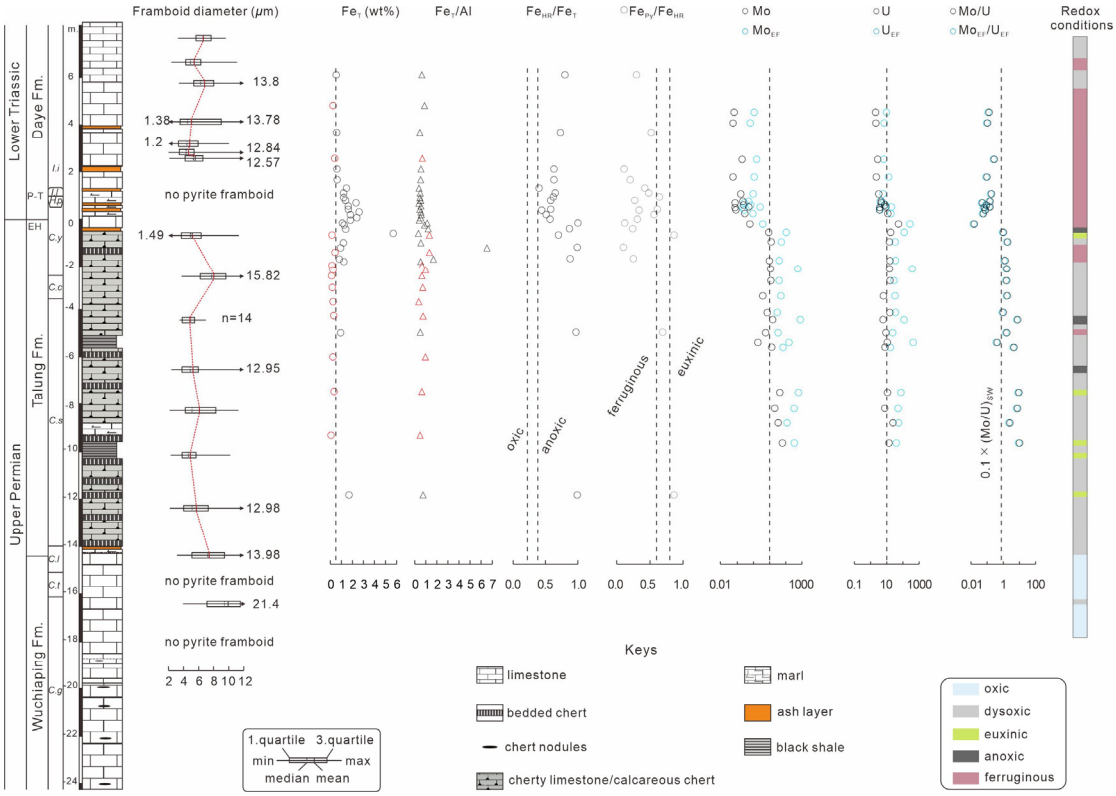

794

795 Figure 5. Stratigraphic log of the Chibi section with total iron (Fe_T), Fe_T/Al, iron proxies [Fe_{HR}/Fe_T,
796 Fe_{Py}/Fe_{HR}, $(Fe_{Py}+Fe_{ox})/Fe_{HR}$, Fe_{ox}/Fe_{HR}], Mo and U concentrations, enrichment factors (Mo_{EF}, U_{EF}) and
797 their ratios (Mo/U, Mo_{EF}/U_{EF}), and pyrite framboid "box-and-whisker" plots. Data of framboids from
798 Yang et al. (2022).

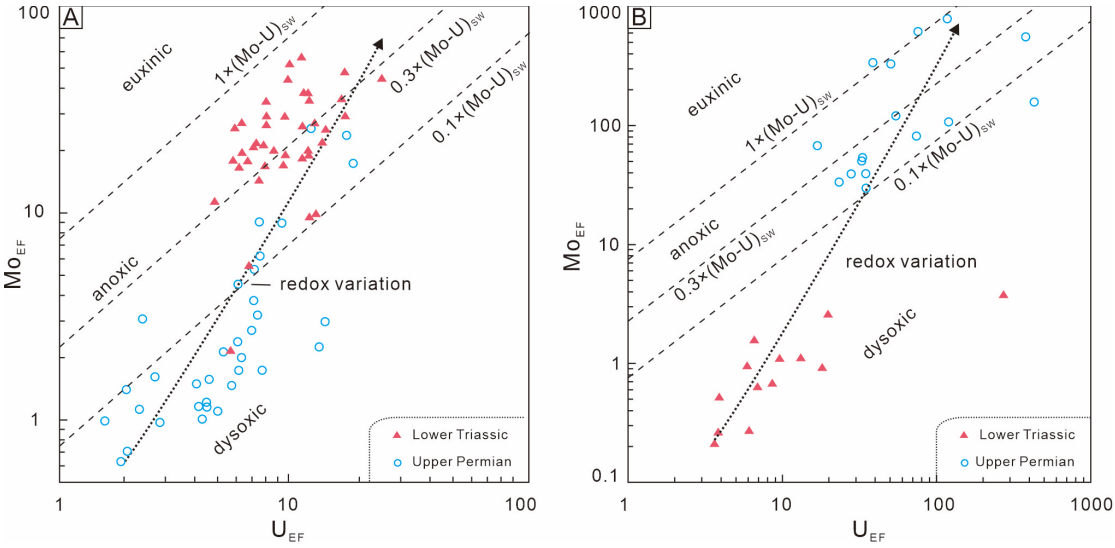

799

800 Figure 6. Covariation of Mo and U across the P-T transition at the Ursula Creek (A) and Chibi (B) section.
801 The "redox variation" pathway represents progressive redox shifts from dysoxic to euxinic conditions
802 (modified from Algeo and Tribovillard, 2009).

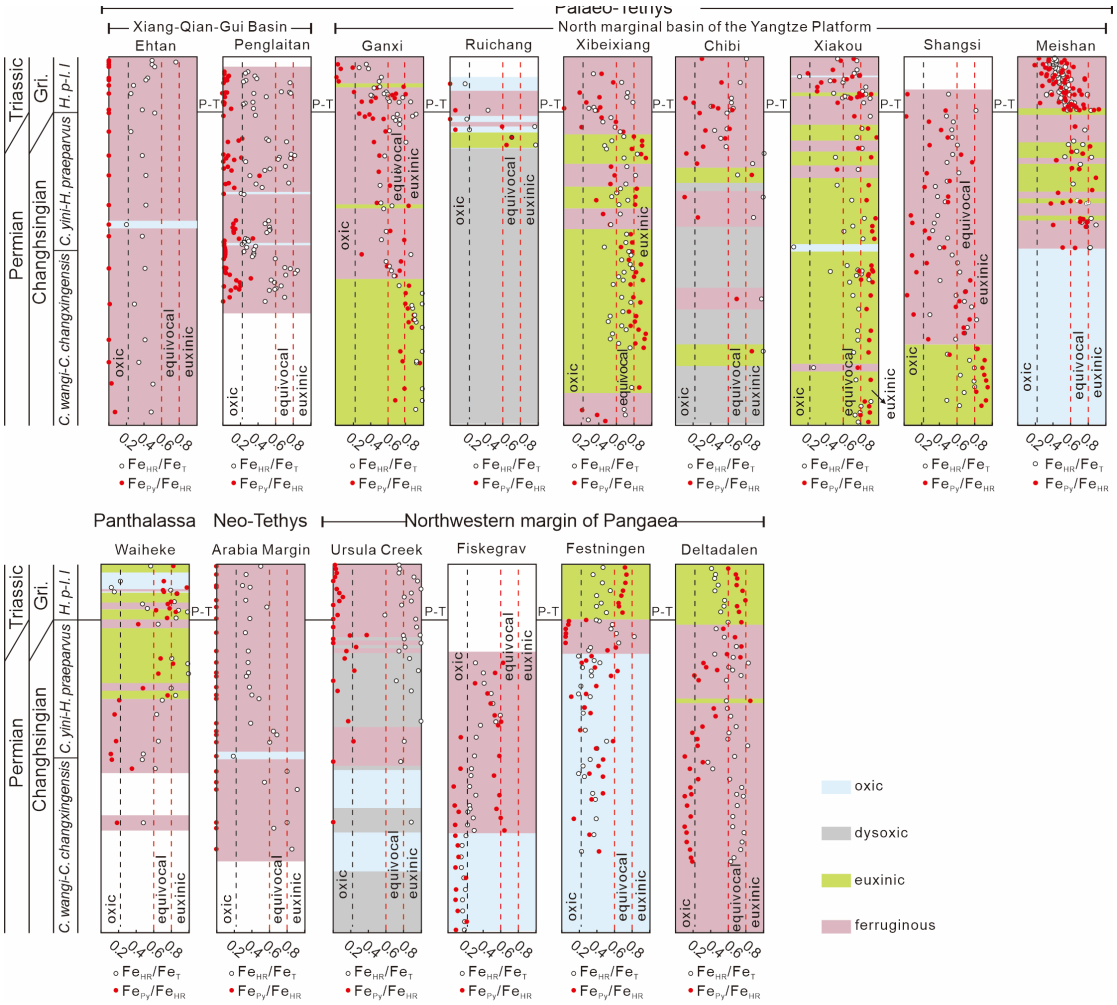

Figure 7. Palaeo-redox reconstruction via iron proxies across various sections situated in different palaeogeographic settings. Data sources: Waiheke, Takahashi et al. (2021); Arabia Margin, Clarkson et al. (2016); Ehtan and Ruichang, Yang et al. (2024); Penglaitan, Xiang et al. (2022); Ganxi, Lei et al. (2017); Xibeixiang, Ge et al. (2022); Xiakou, Shen et al. (2016); Shangsi, Xiang et al. (2016); Meishan, Xiang et al. (2020); Fiskegrav, Mettam et al. (2017); Festningen and Deltadalen, Schobben et al. (2020). Gri. - Griesbachian; *H. p* - *H. parvus*; *I. i* - *I. isarcica*.

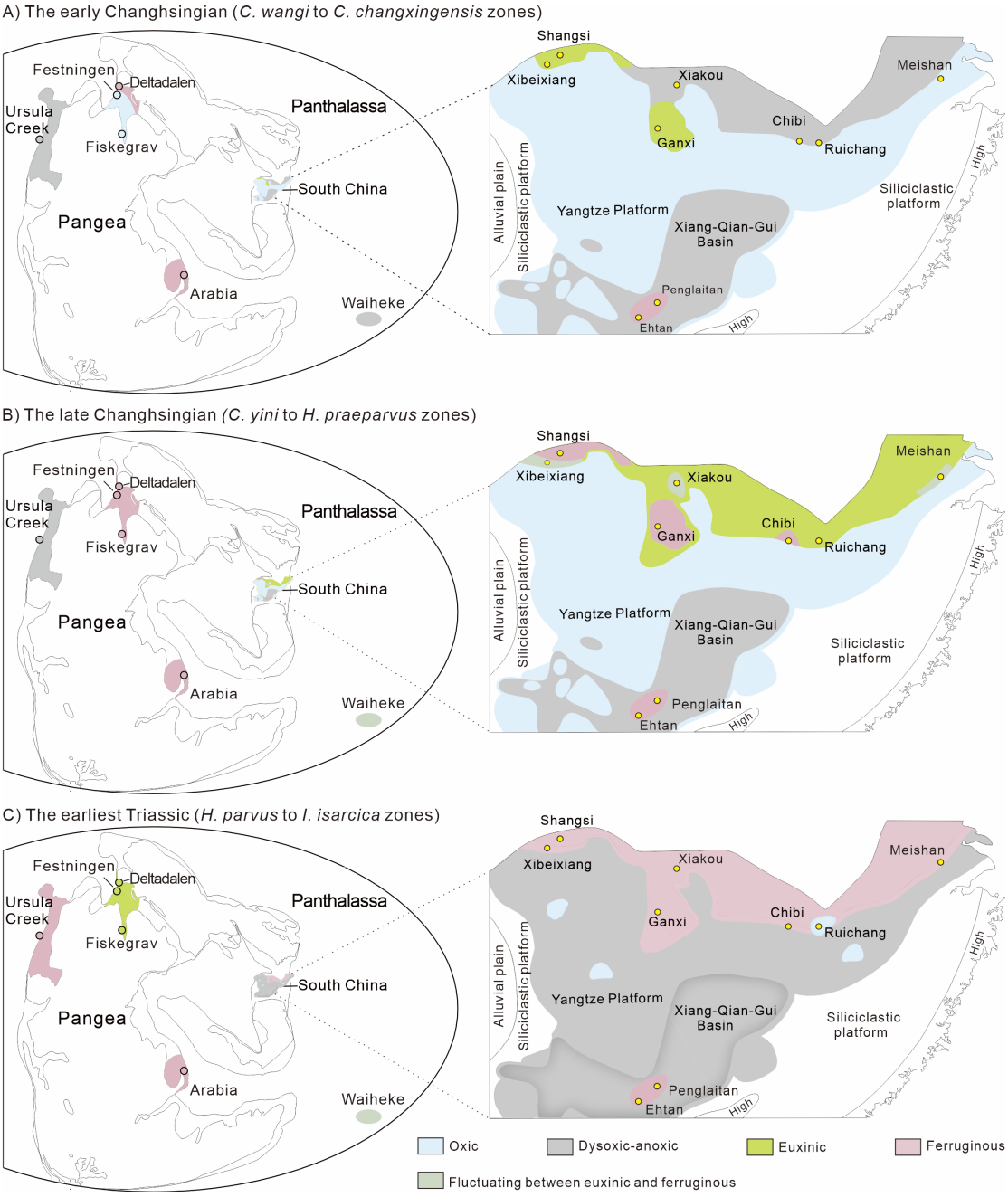

Figure 8. Distribution of ferruginous conditions across the P-T transition, based on the data from Figure 7.